Indian Journal of Chemistry
Vol. 65, February 2026, pp. 61-81
DOI: 10.56042/ijc.v65i2.16089

DFT, wavefunction and toxicity analyses of Megazol

J Jebasingh Kores[a], I Antony Danish[b], T Balasankar[c], D Abiya Chelliah[d], P Jeya Sheela[e], S Darwin Paul Edison[d] & J Winfred Jebaraj*[f]

[a] Department of Physics, Pope's College[#] (Autonomous), Sawyerpuram 628 251, Tamil Nadu, India

[b] Department of Chemistry, Sadakathullah Appa College[#] (Autonomous), Tirunelveli 627 011, Tamil Nadu, India

[c] Chemistry Section, FEAT, Annamalai University, Chidambaram 608 001, Tamil Nadu, India

[d] Department of Botany, St. John's College[#], Tirunelveli 627 002, Tamil Nadu, India

[e] Department of Microbiology, Sadakathullah Appa College[#] (Autonomous), Tirunelveli 627 011, Tamil Nadu, India

[f] Department of Chemistry, St. John's College[#], Tirunelveli 627 002, Tamil Nadu, India

E-mail: winfred.chem@stjohnscollege.edu.in

Received 30 December 2024; accepted (revised) 29 January 2026

Megazol is a drug molecule used to treat acid-related diseases of the stomach. The B3LYP/6-311++G(d,p) level of theoretical calculations frequently employs Gaussian 16W software. In the present work electronic structure analysis, FMO, NBO, MEP, Mulliken charge, vibrational frequency analyses, and electronic excitation determination through the IEFPCM model in various solvents have been obtained. NBO analysis explains that this is a stable molecule. By using Multiwfn 3.8 software, NCI, a shaded surface map, and hole electron interaction (HEI) with inter-fragment charge transfer analyses have been determined. In the S6 excited state, electrons can move across π-linkers from an electron donor to an electron acceptor, according to HEI analysis. Heat maps are generated and discussed for the lowest six excitation states. Simulated scanning tunneling microscope analysis has also been performed. Using the Shermo software, the impact of temperature on S, CV and CP has also been ascertained. Theoretical UV-Vis and IR have been discussed. The toxicity of the molecule is explained.

Keywords: Megazol, DFT, Hole-electron transfer, NBO, MEP

Nitroimidazoles are a significant family of nitrogen heterocyles; some of them have a wide range of biological activities, including antimicrobial[1-3], anticancer[4], antiprotozoal[5], antiviral[6,7], antileishmanial[8], antigiardial[9,10], antioxidant[11], anti-inflammatory[12], antiplasmodial[13], and anti-mycobacterial, among others[14-17]. Although nitrogen heterocycles such as benznidazole and nifurtimox have been employed for a long time as radiosensitisers for Chagas disease[18] or misonidazole[19], no significant advancements could be achieved since this class of chemicals was shown to display mutagenicity risk. This also holds true for megazol, a 5-nitroimidazole with a thiadiazole ring molecule that has demonstrated strong curative activity in rats infected with *Trypanosoma brucei*[20] and mice infected with several strains of *Trypanosoma cruzi*[21]. Nevertheless, there are a few reasons to reevaluate the mutagenicity restrictions.

The key finding was that, whereas nitro reductases from *Salmonella typhimurium*, the bacteria employed in the Ames test[22], is required for the mutagenic activation of Megazol, this does not appear to be the case with nitro-reductases[23] from mammals. The second megazol finding is that at least 25,000 new cases of the disease are reported in Africa each year[24]. Hence there is a huge shortage of therapeutic treatment, and trusting in drugs such as asmelarsoprol[25], which have appreciable toxicity, or an important drug like difluoromethylornithine (DFMO) should be administered in high doses[26]. In this context, we considered a detailed study on structural aspects related to its electron density and reactivity of megazol to be very important.

Density Functional Theory (DFT) has recognised itself as a competent method for the study of the structural and vibrational properties of biomolecules since it gives accurate values when compared with the observed values. It offers satisfactory assurance about the results when incorporated into a proper exchange-correlation functional and for comparison[27].

Affiliated to Manonmaniam Sundaranar University, Abishekepatti, Tirunelveli 627 012, India

Computational analysis

The Chemsketch program is used to prepare the title molecule's 2D chemical structure[28]. Next the Avogadro tool is used to morph the 2D structure into a 3D structure with the least amount of energy[29]. Every computation is done in the gaseous phase. The Becke–Lee–Yang–Parr (B3LYP) functionals serve as the main foundation for the DFT calculations. The correlation functional used for the simulations is that of Lee, Yang, and Parr, with both local and non-local terms employing the 6-311++G(d,p) basis set[30], using the Gaussian 16W suite of programs[31], involving gradient-optimized geometry[32]. The exchange functional is a local spin density exchange with Becke gradient correction. The GaussSum 3.0 software provides assurance of perfect optimisation and convergence[33]. The fact that there are no computations for imaginary frequencies indicates that the molecule has reached full convergence and an energy-minimized structure. The VEDA 4.0 tool is used to determine the PED calculations in the IR vibrational analysis[34]. The wave function analyses are performed using Multiwfn 3.8 software[35]. The iso-surfaces generated are viewed by the VMD 1.9.4 tool[36]. The Shermo software calculates how temperature can affect S, CV, and CP[37].

Results and Discussion

Electronic assembly analysis

Table 1 displays the atom list of the headline molecule's energy-minimized structure. Fig. 1 displays the energy minimization and full convergence graphs produced by the GaussSum 3.0 program in addition to the 2D and energy-minimized 3D structures.

The bond distance, bond angle, and dihedral angles of the optimized structure are shown in Table 2. The bond length is defined as "the average distance between the nuclei of two bonded atoms in a molecule". The bond distance for the title molecule is examined using the basis set provided. Table 2 reveals that the shortest bond distance is found between 11N-17H (1.007 Å), slightly shorter than the actual bond length of 1.12 Å. The longest bond distance is located at 2S-4C (1.770 Å) which is slightly longer than the

Table 1 — The optimized structure's atom list of megazol

1	2	3	4	5	6	7
C	S	N	C	N	C	N
8	9	10	11	12	13	14
N	C	C	N	C	N	O
15	16	17	18	19	20	21
O	H	H	H	H	H	H

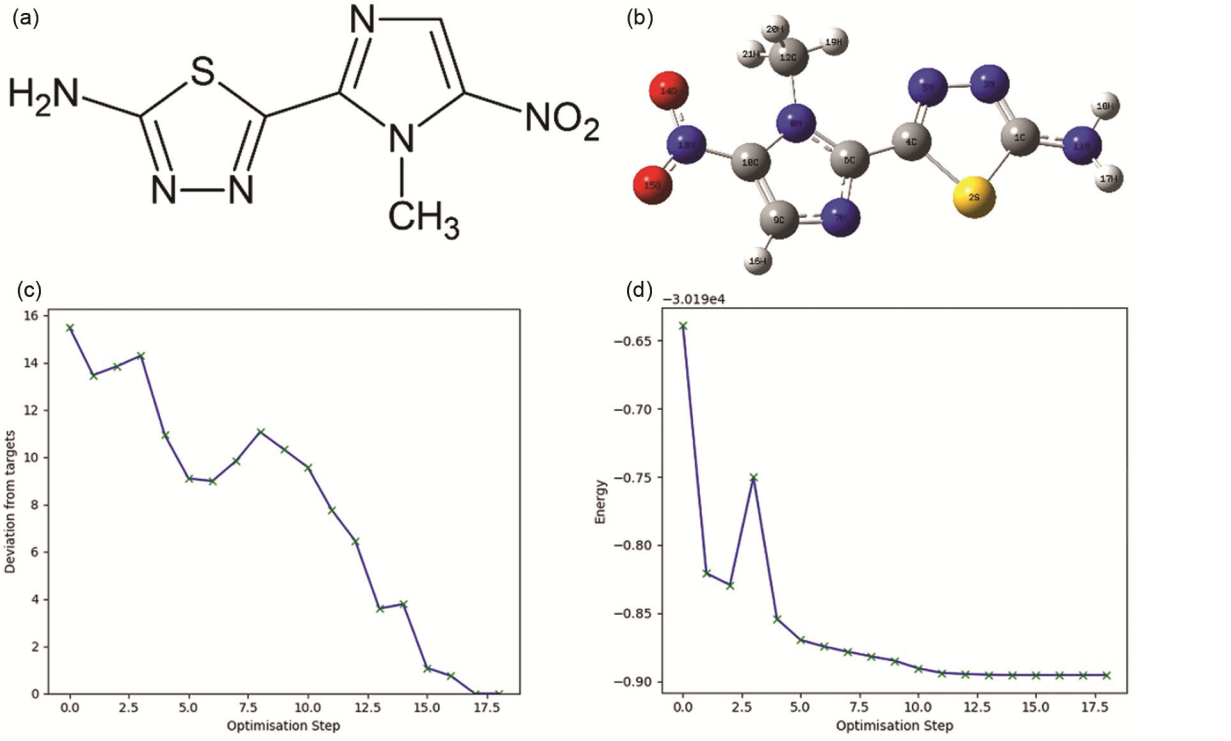

Fig. 1 — (a) 2D (b) 3D (c) whole optimisation (d) perfect convergence of the converged optimised molecule by the B3LYP/6-311++ G(d,p) basis set.

Table 2 — Geometric parameters of optimised megazol

S. No	Atom set	Bond distance (Å)	Atom set	Bond angle (°)	Atom set	Dighedaral angle (°)	Planarity
1	1C-2S	1.754	2S-1C-3N	114.6	3N-1C-2S-4C	–0.2	–SP
2	1C-3N	1.311	2S-1C-11N	122.7	11N-1C-2S-4C	–177.0	–AP
3	1C-11N	1.365	3N-1C-11N	122.6	2S-1C-3N-5N	–0.1	–SP
4	2S-4C	1.770	1C-2S-4C	85.4	11N-1C-3N-5N	176.7	+AP
5	3N-5N	1.357	1C-3N-5N	112.3	2S-1C-11N-17H	–27.8	–SC
6	4C-5N	1.299	2S-4C-5N	113.4	2S-1C-11N-18H	–170.7	–AP
7	4C-6C	1.452	2S-4C-6C	118.9	3N-1C-11N-17H	155.6	+AP
8	6C-7N	1.337	5N-4C-6C	127.7	3N-1C-11N-18H	12.8	+SP
9	6C-8N	1.366	3N-5N-4C	114.3	1C-2S-4C-5N	0.5	+SP
10	7N-9C	1.347	4C-6C-7N	120.5	1C-2S-4C-6C	–179.4	–AP
11	8N-10C	1.387	4C-6C-8N	127.2	1C-3N-5N-4C	0.5	+SP
12	8N-12C	1.473	7N-6C-8N	112.4	2S-4C-5N-3N	–0.7	–SP
13	9C-10C	1.381	6C-7N-9C	106.2	6C-4C-5N-3N	179.2	+AP
14	9C-16H	1.078	6C-8N-10C	104.6	2S-4C-6C-7N	–0.3	–SP
15	10C-13N	1.426	6C-8N-12C	127.5	2S-4C-6C-8N	179.6	+AP
16	11N-17H	1.007	10C-8N-12C	127.9	5N-4C-6C-7N	179.8	+AP
17	11N-18H	1.011	7N-9C-10C	109.4	5N-4C-6C-8N	–0.2	–SP
18	12C-19H	1.085	7N-9C-16H	123.4	4C-6C-7N-9C	179.9	+AP
19	12C-20H	1.088	10C-9C-16H	127.2	8N-6C-7N-9C	0.0	+SP
20	12C-21H	1.088	8N-10C-9C	107.5	4C-6C-8N-10C	–180.0	–AP
21	13N-14O	1.232	8N-10C-13N	125.2	4C-6C-8N-12C	0.0	+SP
22	13N-15O	1.229	9C-10C-13N	127.3	7N-6C-8N-10C	0.0	+SP
23			1C-11N-17H	118.9	7N-6C-8N-12C	179.9	+AP
24			1C-11N-18H	114.8	6C-7N-9C-10C	0.0	+SP
25			17H-11N-18H	115.5	6C-7N-9C-16H	180.0	+AP
26			8N-12C-19H	107.7	6C-8N-10C-9C	0.0	+SP
27			8N-12C-20H	109.5	6C-8N-10C-13N	–179.9	–AP
28			8N-12C-21H	109.5	12C-8N-10-9C	–179.9	–AP
29			19H-12C-20H	110.7	12C-8N-10-13N	0.1	+SP
30			19H-12C-21H	110.7	6C-8N-12C-19H	–0.2	–SP
31			20H-12C-21H	108.7	6C-8N-12C-20H	–120.7	–AP
32			10C-13N-14O	118.6	6C-8N-12C-21H	120.2	+AC
33			10C-13N-15O	116.6	10C-8N-12C-19H	179.7	+AP
34			14O-13N-15O	124.8	10C-8N-12C-20H	59.2	+SC
35					10C-8N-12C-21H	–59.8	–SC
36					7N-9C-10C-8N	0.0	+SP
37					7N-9C-10C-13N	179.9	+AP
38					16H-9C-10C-8N	–180.0	–AP
39					16H-9C-10C-13N	0.0	+SP
40					8N-10C-13N-14O	0.1	+SP
41					8N-10C-13N-15O	–179.9	–AP
42					9C-10C-13N-14O	–179.8	–AP
43					9C-10C-13N-15O	0.2	+SP

actual value of 1.63 Å. “The bond angle can be defined as the angle formed between two covalent bonds that originate from the same atom”. The bond angle of the headline molecule is studied and shown in Table 2. From that, it is clear that the shortest bond angle is placed at 1C-2S-4C (85.4°), while the largest angle is present at 10C-8N-12C (127.9°). Table 2 also provides the dihedral angle for the molecule under inquiry. In this molecule, planarities like synperiplanar, synclinical, and antiperiplanar are

observed. Every theoretical estimate is in good agreement with the previous studies[38,39].

Mulliken charge analysis

Table 3 displays the Mulliken charge for the headline molecule, which is determined at the same level of theory. Fig. 2 displays the figure that is produced. It is evident from Table 3 and Fig. 2 that every carbon atom has a negative charge, with the exception of 4C and 9C. 1C and 12C have almost the same charge, while 9C has a high positive value. Except for 3N, all other nitrogen atoms have negative charges. The two oxygen atoms have positive charges. 2S has a positive charge on it. Positive charge is present in every hydrogen atom. The methyl protons have the same charge, while one of the hydrogens attached to the NH_2 group has a high value.

Table 3 — Mulliken charge distribution of the optimized structure of megazol

Atom	Charge (a.u.)	Atom	Charge (a.u.)
1C	–0.4525	12C	–0.4406
2S	0.0979	13N	–0.3925
3N	0.1990	14O	0.0040
4C	0.2526	15O	0.0136
5N	–0.3388	16H	0.2433
6C	–0.3788	17H	0.2568
7N	–0.0259	18H	0.2769
8N	–0.0563	19H	0.2045
9C	0.6621	20H	0.2049
10C	–0.3136	21H	0.2062
11N	–0.2230		

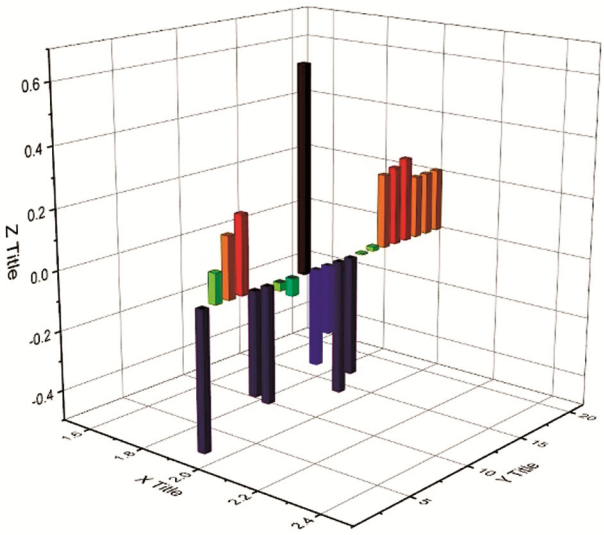

Fig. 2 — Mulliken charge plot for megazol

Electrostatic potential analysis

Analyzing a three-dimensional representation of the molecular electrostatic potential (MEP) surface allows for the observation of its surface on the isoelectronic density surface. It provides insight into the molecule's reactive regions. The size, shape, and electrostatic potential value of molecules are expressed by their surface. Within the applied color scheme, a location with a high electron density (negative charge) is shown by the color red, while a region with a low electron density (positive charge) is indicated by the color blue. Green denotes a neutral zone, yellow a slightly electron-rich region, and light blue a slightly electron-deficient region[40]. The following formula is used to get the molecular electrostatic potential values for the systems under study[41]:

$$V(r) = \sum \frac{Z_A}{|R_A - r|} - \int \frac{\rho(r')}{|r' - r|} dr \quad \ldots(1)$$

For the headline molecule, MEP is determined by the same method and shown in Fig. 3. From Fig. 3, it is clear that the electron-rich area (red color) is located on the oxygen atoms bonded to nitrogen atom, and a blue color domain is seen around the hydrogen atoms attached to nitrogen atoms (NH_2). The hydrogen atoms bound to the nitrogen atom have the greatest positive area (blue), which may be a potential nucleophilic target.

Frontier molecular orbital determination

DFT is a powerful framework for the investigation of chemical reactivity. Including details regarding a molecular system's optical, electrical, and anti-corrosion qualities is also helpful[42]. The title molecule's LUMO and HOMO are calculated using the DOS spectrum and B3LYP/6-311++G(d,p) level

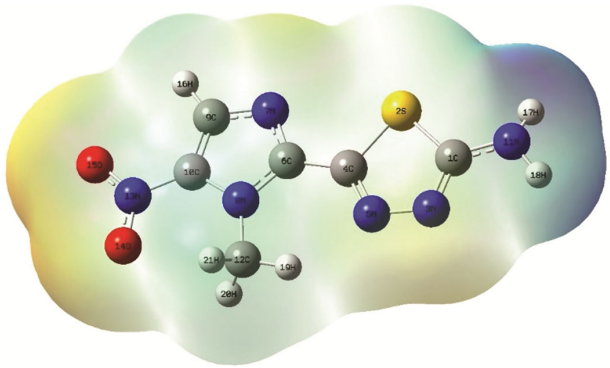

Fig. 3 — ESP diagram for the title molecule

of theory, as shown in Fig. 4. It is clear from Fig. 4 that the LUMO is distributed throughout the molecule, whereas the HOMO extends across the chemical structure with the exception of the methyl group.

The HOMO, LUMO, and energy gaps are found to be -6.7457, -3.0367, and 3.709 eV. Since the energy gap is low, this molecule can donate electrons easily. The other properties are calculated from the HOMO and LUMO values, which are calculated and given in Table 4. It is noticed that the electron-donating capability (ω^-) is higher than the electron-accepting capability (ω^+) which also confirms that this molecule can donate electrons easily. The ionisation potential (I), electron affinity (A), electronegativity (χ), and chemical potential (μ) are calculated as 6.7457, 3.0367, 4.8912, and -4.8912 eV, respectively. This molecule is hard since the chemical hardness value (1.8545 eV) is higher than the chemical softness (S) (0.5392 eV). The other parameters are also calculated and shown in Table 4.

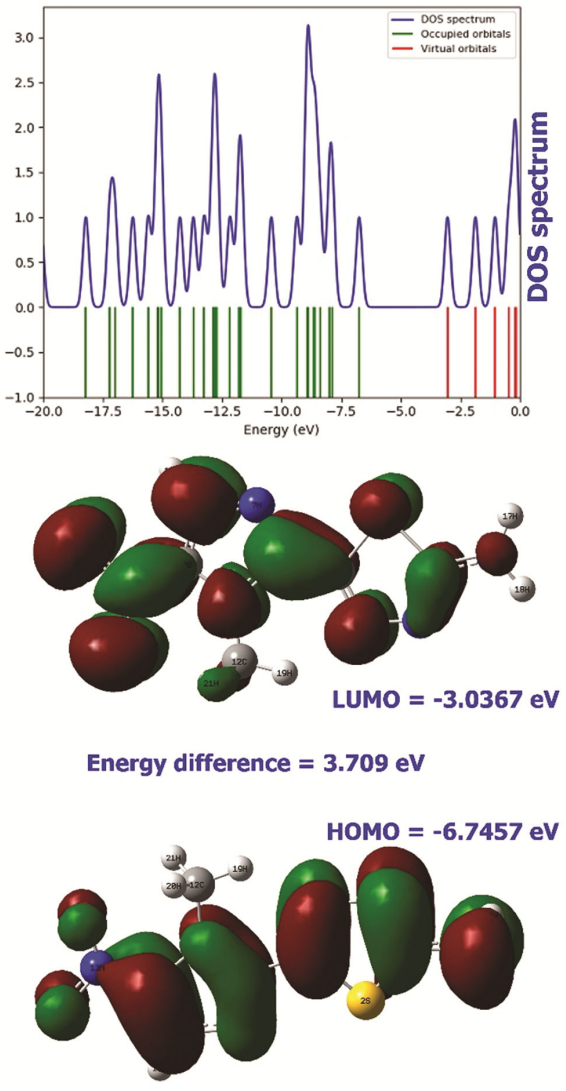

Fig. 4 — DOS spectrum and HOMO – LUMO for the investigated molecule.

NBO interpretation

Natural bond orbital (NBO) analysis accurately determines a molecule's Lewis structure by utilizing the maximum proportion of an orbital's electron density[44]. Due to knowledge of interactions between filled and virtual orbitals, it is often a more sensitive approach for calculating intra- and intermolecular interactions[45]. This method extracts data on charge densities variations in bonding and anti-bonding

Table 4 — Chemical reactivity parameters for megazol

S. No.	Parameter	Formulae [Ref. 43]	Charge (eV)
1	HOMO		–6.7457
2	LUMO		–3.0367
3	Energy gap (ΔE)	$E_{LUMO} - E_{HOMO}$	3.7090
4	Ionisation potential (I)	$I = - E_{HOMO}$	6.7457
5	Electron affinity (A)	$A = - E_{LUMO}$	3.0367
6	Electronegativity (χ)	$\chi = \frac{I+A}{2}$	4.8912
7	Chemical potential (μ)	$\mu = - (\chi)$	-4.8912
8	Chemical hardness (η)	$\eta = \frac{I-A}{2}$	1.8545
9	Chemical softness (S)	$S = \frac{1}{\eta}$	0.5392
10	Electrophilicity index (ω)	$\omega = \frac{\mu^2}{2\eta}$	6.4502
11	Electron accepting capability (ω^+)	$\omega^+ = \frac{(I+3A)^2}{16(I-A)}$	4.2364
12	Electron donating capability (ω^-)	$\omega^- = \frac{(3I+A)^2}{16(I-A)}$	9.1276
13	Global softness (s)	$s = \frac{1}{2\eta}$	0.2696
14	$\Delta E_{Back\ donation}$	$\Delta E = \frac{-\eta}{4}$	–0.4636
15	Nucleophilicity index (N)	$N = \frac{1}{\omega}$	0.155
16	Additional electronic charge (ΔN_{max})	$\Delta N_{max} = \frac{-\mu}{\eta}$	2.6375
17	Optical softness (σ_0)	$\sigma_o = \frac{1}{\Delta E}$	0.2696

orbitals of proton donors and acceptors. The stabilization energy E(2) associated with i-j delocalization is estimated for each donor (i) and acceptor (j) and defined as:

$$E_2 = \Delta E_{i,j} = q_i \frac{F(i,j)^2}{\varepsilon_j - \varepsilon_i} \quad \ldots(2)$$

"Where q_i is the donor orbital occupancy; E_i and E_j are the diagonal elements; and F(i,j) is the off-diagonal NBO Fock matrix element". The E(2) value indicates the intensity of the interaction between electron donors and acceptors. If E(2) is larger, the intensity of interaction is also larger[46,44]. The theoretical level of the NBO analysis for the target molecule is computed and presented in Table 5. For this molecule, σ → σ*, σ → π*, π → π*, LP → σ*, and LP → π* interactions are reported in a chosen manner in Table 5.

Table 5 — Second-order perturbation theory analysis

S. No	Type	Donor NBO (i)	ED/e (a.u.)	Type	Acceptor NBO(j)	ED/e (a.u.)	E(2) (kcal/mol)	E(j)-E(i) (a.u.)	F(i,j) (a.u.)
1.	σ	C1-S2	1.9760	σ*	C4-C6	0.0363	3.91	1.12	0.059
1.	σ	C1-S2	1.9760	σ*	N11-H18	0.0098	2.75	1.07	0.049
3.	π	C1-N3	1.8601	π*	C4-N5	0.3618	15.11	0.32	0.066
5.	σ	S2-C4	1.9713	σ*	C1-N11	0.0242	5.90	1.10	0.072
5.	σ	S2-C4	1.9713	σ*	C6-N8	0.0422	4.60	1.10	0.064
6.	σ	N3-N5	1.9784	σ*	C1-N11	0.0242	4.66	1.28	0.069
6.	σ	N3-N5	1.9784	σ*	C4-C6	0.0363	4.16	1.29	0.066
8.	π	C4-N5	1.8927	π*	C1-N3	0.4015	9.02	0.32	0.052
8.	π	C4-N5	1.8927	π*	C6-N7	0.4692	10.83	0.34	0.060
11.	π	C6-N7	1.7598	π*	C4-N5	0.3620	13.13	0.30	0.058
11.	π	C6-N7	1.7598	π*	C9-C10	0.3664	27.37	0.32	0.086
12.	σ	C6-N8	1.9807	σ*	C10-N13	0.0875	4.83	1.16	0.068
12	σ	C6-N8	1.9807	σ*	N8-C10	0.0335	1.76	1.25	0.042
13.	σ	N7-C9	1.9790	σ*	C4-C6	0.0363	4.95	1.26	0.071
13.	σ	N7-C9	1.9790	σ*	C10-N13	0.0875	4.77	1.13	0.067
14.	σ	N8-C10	1.9820	σ*	C4-C6	0.0363	4.12	1.27	0.065
15.	σ	N8-C12	1.9892	σ*	N13-O15	0.0547	14.76	3.27	0.198
15.	σ	N8-C12	1.9892	π*	N13-O15	0.6706	9.88	4.31	0.225
16.	σ	C9-C10	1.9796	σ*	N8-C12	0.0188	4.90	1.04	0.064
17.	π	C9-C10	1.7327	π*	C6-N7	0.4692	12.86	0.29	0.058
20.	σ	N11-H17	1.9847	σ*	C1-N3	0.0316	4.02	1.22	0.063
21.	σ	N11-H18	1.9813	σ*	C1-S2	0.0777	6.24	0.85	0.066
22.	σ	C12-H19	1.9873	σ*	N8-C10	0.0337	4.56	0.93	0.059
22.	σ	C12-H19	1.9873	π*	N13-O15	0.6706	5.96	4.08	0.170
23.	σ	C12-H20	1.9848	σ*	N13-O14	0.0578	4.38	1.11	0.063
23.	σ	C12-H20	1.9848	π*	N13-O15	0.6706	20.57	4.07	0.315
24.	σ	C12-H21	1.9847	σ*	N13-O15	0.0547	12.00	3.03	0.172
24.	σ	C12-H21	1.9847	π*	N13-O15	0.6706	34.21	4.07	0.406
27.	π	N13-O15	1.9856	LP(3)	O14	1.4763	11.48	0.17	0.076
27.	π	N13-O15	1.9856	π*	C9-C10	0.3664	4.31	0.45	0.043
48.	LP(2)	S2	1.6510	π*	C1-N3	0.4015	29.67	0.24	0.077
48.	LP(2)	S2	1.6510	π*	C4-N5	0.3620	25.12	0.25	0.071
49.	LP(1)	N3	1.9054	σ*	C1-S2	0.0777	14.34	0.57	0.081
49.	LP(1)	N3	1.9054	σ*	C4-N5	0.0275	5.74	0.94	0.067
50.	LP(1)	N5	1.8931	σ*	C1-N3	0.0316	5.39	0.93	0.064
50.	LP(1)	N5	1.8931	σ*	S2-C4	0.0746	15.35	0.56	0.083

(*Contd.*)

Table 5 — Second-order perturbation theory analysis (*Contd.*)

S. No	Type	Donor NBO (i)	ED/e (a.u.)	Type	Acceptor NBO(j)	ED/e (a.u.)	E(2) (kcal/mol)	E(j)-E(i) (a.u.)	F(i,j) (a.u.)
51.	LP(1)	N7	1.9206	σ*	C6-N8	0.0422	7.97	0.82	0.073
51.	LP(1)	N7	1.9206	σ*	C9-C10	0.0216	4.80	0.93	0.060
52.	LP(1)	N8	1.5241	π*	C6-N7	0.4692	49.89	0.28	0.106
52.	LP(1)	N8	1.5241	π*	C9-C10	0.3664	32.44	0.28	0.088
53.	LP(1)	N11	1.7950	π*	C1-N3	0.4015	40.37	0.29	0.101
54.	LP(1)	O14	1.9826	σ*	C10-N13	0.0875	4.39	1.12	0.064
55.	LP(2)	O14	1.8996	σ*	C10-N13	0.0875	9.87	0.61	0.070
56.	LP(3)	O14	1.4763	π*	N13-O15	0.6706	5.68	3.83	0.137
57.	LP(1)	O15	1.9823	σ*	C10-N13	0.0875	4.01	1.12	0.061
58.	LP(2)	O15	1.8938	σ*	C10-N13	0.0875	10.80	0.61	0.073
58.	LP(2)	O15	1.8938	σ*	N13-O14	0.0578	14.64	0.87	0.102

"E(2) is the energy of hyper conjugative interaction (stabilization energy)
E(j)-E(i) is the energy difference between donor and acceptor i and j NBO orbitals
F(i,j) is the Fock matrix element between i and j NBO orbitals
ED/e is the electron density of donor and acceptor NBO orbitals
LP(n)A is a valence lone pair orbital (n) on A atom"

The interactions of σ(N8-C12) → σ*(N13-O15), σ(C12-H21) → σ*(N13-O15), and σ(N11-H18) → σ*(C1-S2) are responsible for the stabilisation with energies of 14.76, 12.00, and 6.24 kcal/mol, respectively. 34.21 and 20.57 kcal/mol are due to the transition of σ(C12-H21) → π*(N13-O15), and σ(C12-H20) → π*(N13-O15) transitions respectively. The interactions of π(C6-N7) → π*(C9-C10), π(C1-N3) → π*(C4-N5), and π(C6-N7) → π*(C4-N5) stabilizes with energy of 27.37, 15.11, and 13.13 kcal/mol respectively. The LP (1) N5 → σ* (S2-C4) and LP (2) O15 → σ*(N13-O14) are responsible for stabilizing the energies of 15.35 and 14.64 kcal/mol respectively. The LP (1) N8 → π* (C6-N7) and LP (1) N11 → π*(C1-N3) helped with the stabilization energies of 49.89 and 40.37 kcal/mol, respectively.

This molecule is interesting in that it has electron acceptors and donors at both ends. They are interconnected by π-linkers (aromatic five-membered ring systems). Hence, there is a chance for the electron transfer from one end to the other. The energy of stabilization is retrieved from Table 5. Initially, LP (1) N11 and σ(N11-H17) donors transfer electrons to the acceptor σ* (C1-N3) with stabilization energies of 40.37 and 4.02 kcal/mol, respectively. 15.11 kcal/mol energy is calculated for the transition of electrons from π(C1-N3) → π*(C4-N5). The π(C4-N5) → π*(C6-N7) transition is stabilized at 10.83 kcal/mol. The donor to acceptor transition [π(C6-N7) → π*(C9-C10)] involves a stabilization energy of 27.37, kcal/mol and meanwhile, 4.12 kcal/mol energy is stabilized for the transition of electrons from σ(N8-C10) → σ*(N8-C10) with a stabilisation energy of 1.76 kcal/mol. The σ(N8-C12) → σ*(N13-O15) transition is stabilized at 14.76 kcal/mol whereas the σ(N8-C12) → π*(N13-O15) transition is stabilized at 9.88 kcal/mol. This is a clear picture that confirms the electronic transition from the donor to the acceptor through the π-linkers.

Fukui function analysis

The concept of the Fukui function is proposed by Parr and Yang[47]. Fukui function (FF) is helpful to have an idea about reactivity indices. They postulate information about which atoms in a molecule can either lose or gain electrons. They are otherwise called cites of nucleophilic attacks or electrophilic attacks. The electron density ρ(r) is the partial derivative of the electron density with respect to the total number of electrons (N) in a system at a constant external potential ν(r). It is defined as:

$$f(r) = \left(\frac{\delta \rho(r)}{\delta(N)} \right)_{\nu(r)} \quad \ldots(3)$$

The Fukui function f_k^+, also known as the index of nucleophilic assault, is present when molecule earnings an electron. The Fukui function f_k^-, also known as the index of electrophilic assault, is present

when a molecule gives an electron[48]. Condensed Fukui functions quantify the likelihood of each atom in a chemical system acting as a reactive site, providing a numerical value. The condensed Fukui function corresponds to electrophilic, nucleophilic, and radical attacks, which are represented by:

$$f^{+}(r) = qk(N+1) - qk(N) \quad \ldots(4)$$

$$f^{-}(r) = qk(N) - qk(N-1) \quad \ldots(5)$$

$$f^{0}(r) = \left[\frac{qk(N+1) - qk(N-1)}{2}\right] \quad \ldots(6)$$

"Where qk is the electronic population of atom k in the (N) neutral, (N-1) cationic, and (N+1) anionic states". For nucleophilicity and electrophilicity, the descriptor Δf(r) is proposed by Morrel *et. al.,* and is well-defined as[49]:

$$\Delta f(r) = [f_k^{+} - f_k^{-}] \quad \ldots(7)$$

The site is prone to electrophilic attack if Δf(r) > 0, and then the site is possible for nucleophilic attack if the condition is if Δ(f) < 0. The dual descriptor, which may be used to ascertain the kind of reactive sites, can be explained using this way.

The electronic population of the headline molecule is determined using Mulliken population analysis (MPA) and Natural population analysis (NPA) using the same functional framework. The Fukui Functions values for cation, anion and neutral species and Δf(r) charges are tabulated in Table 6. From the data, a pictorial representation is created and shown in Fig. 5. In the NPA calculation, 13N > 1C is common for cationic species, anionic moiety, and neutral group. The order of reactivity is 13N > 1C > 6C > 17H > 18H > 16H > 21H > 20H > 9C > 2S > 5N (cationic); 13N > 1C > 6C > 17H > 18H > 16H > 21H > 20H > 9C > 5N > 19H (neutral); and 13N > 1C > 17H > 6C > 18H > 16H > 21H > 20H > 4C > 19H > 10C (anionic). For cationic and neutral species, nucleophilic attack is possible at 13N, while for anionic species, electrophilic attack is possible at 11N. According to MPA calculations, nucleophilic attack is possible for cationic, neutral, and anionic species at 10C, 9C, and 13N, respectively. The duel descriptor calculations reveal that except for 1C, 8N, and 13N, all other atoms will have a chance for nucleophilic attack since they have positive values. In this case, 11N (0.3308 a.u.) will be the best region for nucleophilic attack.

Table 6 — The Fukui functions (f_k^{+}), (f_k^{-}), ($f^{0}(r)$) and Δf(r) for the title molecule

S. No	Atoms	Natural population analysis (NPA) (a.u.)				Mulliken population analysis (MPA) (a.u.)		
		f^{+}	f^{0}	f^{-}	Δf(r)	f^{+}	f^{0}	f^{-}
1	1C	0.5315	0.6171	0.6754	–0.1439	0.0419	–0.4525	0.0610
2	2S	0.0595	–0.0660	–0.2213	0.2808	–0.0377	0.0979	0.0459
3	3N	–0.3590	–0.5119	–0.5862	0.2272	0.1944	0.1990	–0.0374
4	4C	0.0247	–0.0370	0.0014	0.0233	0.0774	0.2526	0.0337
5	5N	0.0493	0.0050	–0.0655	0.1148	0.1063	–0.3388	0.1404
6	6C	0.4464	0.4309	0.3450	0.1014	0.0650	–0.3788	0.0895
7	7N	–0.4075	–0.4424	–0.4600	0.0525	0.0317	–0.0259	–0.0474
8	8N	–0.0670	–0.0311	–0.0486	–0.0184	0.0105	–0.0563	0.1176
9	9C	0.1212	0.0200	–0.0991	0.2203	0.0408	0.6621	0.0890
10	10C	0.0192	–0.1007	–0.0469	0.0661	0.2381	–0.3136	–0.0171
11	11N	–0.5244	–0.7713	–0.8552	0.3308	0.2191	–0.2230	0.0127
12	12C	–0.0964	–0.1349	–0.1047	0.0083	0.0032	–0.4406	–0.0061
13	13N	0.7381	0.7918	0.7605	–0.0224	–0.0225	–0.3925	0.1705
14	14O	–0.3804	–0.4651	–0.6421	0.2617	–0.0046	0.0040	0.1640
15	15O	–0.3703	–0.4665	–0.6559	0.2856	0.0521	0.0136	0.1682
16	16H	0.1778	0.1682	0.1483	0.0295	–0.0051	0.2433	–0.0024
17	17H	0.3695	0.3667	0.3480	0.0215	–0.0047	0.2568	0.0088
18	18H	0.3624	0.3610	0.3422	0.0202	–0.0065	0.2769	–0.0002
19	19H	0.0078	–0.0021	–0.0392	0.0470	–0.0009	0.2045	–0.0006
20	20H	0.1446	0.1296	0.0973	0.0473	0.0008	0.2049	0.0049
21	21H	0.1532	0.1387	0.1065	0.0467	0.0009	0.2062	0.0050

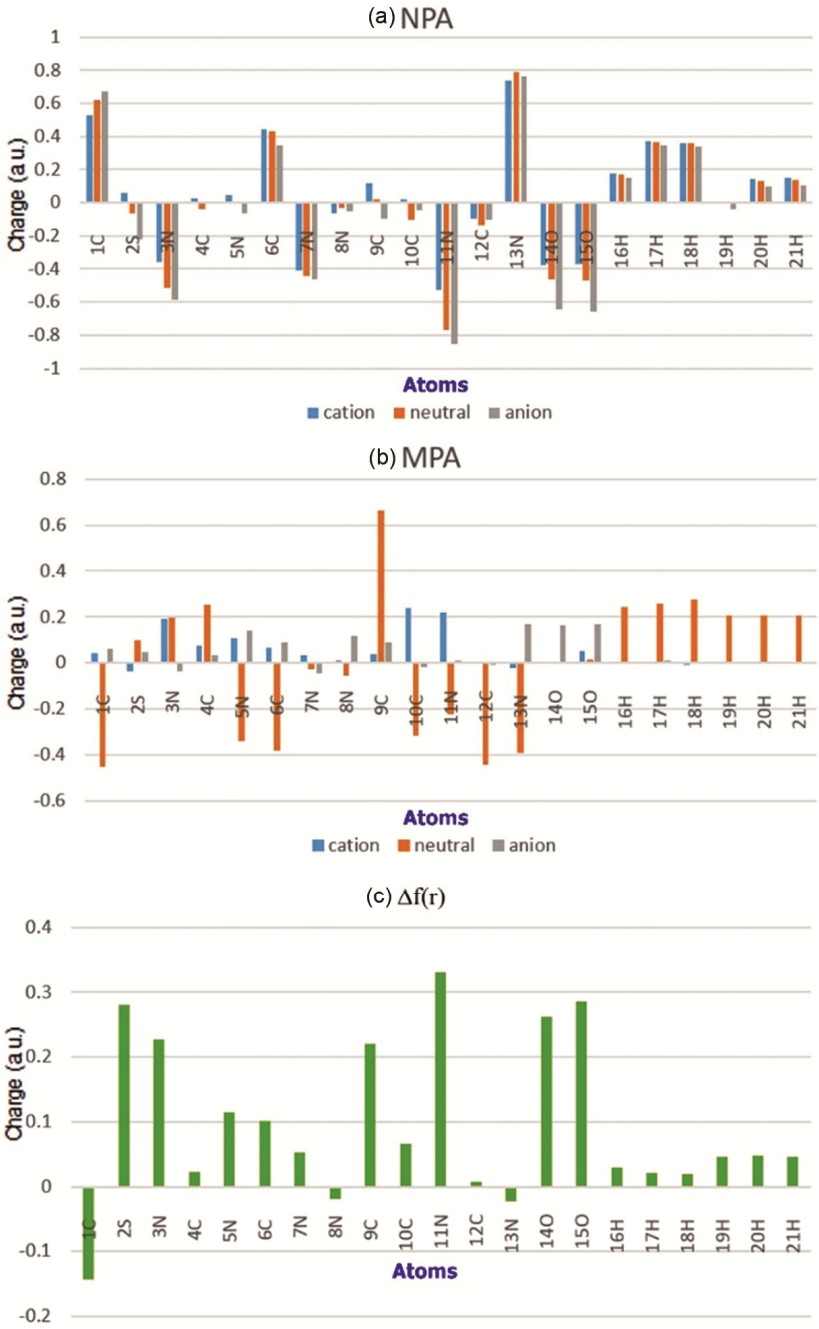

Fig. 5 — (a) Natural Population Analysis (b) Mulliken Population Analysis and (c) Δf(r) Fukui function values for megazol

Study of weak interaction

The Multiwfn 3.8 software can be used to examine weak interactions like the steric effect and the van der Waals force of attraction of a molecule. The atoms in a molecule (AIM) hypothesis can help us understand the weak interactions that take place inside molecules. The reduced density gradient (RDG) iso-surface function is utilized to calculate non-covalent interactions, as defined as:

$$RDG(r) = \frac{1}{2(3\pi^2)^{1/3}} \frac{|\nabla\rho(r)|}{\rho(r)^{4/3}} \quad \ldots(8)$$

The reduced density gradient (RDG) is plotted against the sign of λ_2, multiplied by the density ρ, results in the NCI plot. The spikes in the low-density gradient zone are shown in Fig. 6. It is a well-known non-covalent interaction trace that becomes more intense as it gets away from zero[50].

It is clear from Fig. 6(a) that there is a van der Waals force (vdW) of attraction at work since the spikes arise between -0.020 and + 0.0010 a.u. The steric effect is apparent when there are spikes over +0.020 a.u. The Multiwfn 3.8 utility creates and displays cube files (.cub) that are then used by the VMD 1.9.4 application. The steric factor is caused by the red-colored spheres inside the two aromatic five membered rings, as shown by the visualised iso-surface (Fig. 6b). The greenish-red rings indicate that the molecule is influenced by the vdW force of attraction. They may be found, respectively, in the caverns next to $–NO_2$, CH_3, NS, and CH_3.

Shaded surface map with projection of LOL analysis

The Multiwfn 3.8 package provides a comprehensive understanding of this study. It locates the molecule's electron-rich and electron-depletion regions[35]. Schmider and Becke define the LOL function as a tool used to identify high localization zones in a specific area[51]. It has the following definition:

$$\mathrm{LOL}(r) = \frac{\tau(r)}{1+\tau(r)} \qquad \ldots(9)$$

"Where $\tau(r)$ (dimensionless variable) is $g_0(r)$ / $g_{(r)}$". It typically depends on the kinetic energy of one positive electron. It is defined as:

$$g(r) = \frac{1}{2}\sum \nabla_{\Psi i}(r)\nabla\psi_i(r) \qquad \ldots(10)$$

"Where Ψ_I (r) is the Hatree-Fock or the Kohn-Sham orbital".

The greater the LOL, the more probable it is that the electron transport in that specific region of the molecule is regulated. The localized orbital locator (LOL) projection is utilized to evaluate the map of the molecule being surveyed *via* the NH_2 and NO_2 sides, as depicted in Fig. 7. The blue ring around the

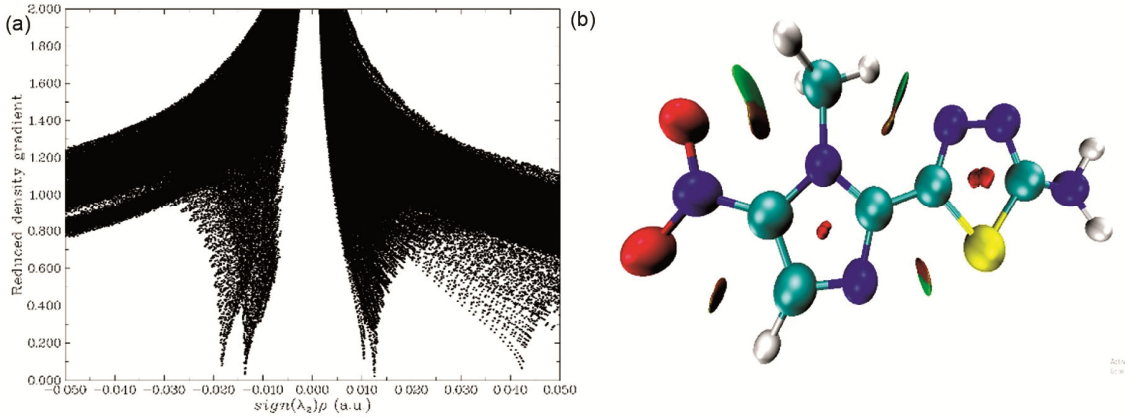

Fig. 6 — (a) The NCI analysis (b) iso-surface function

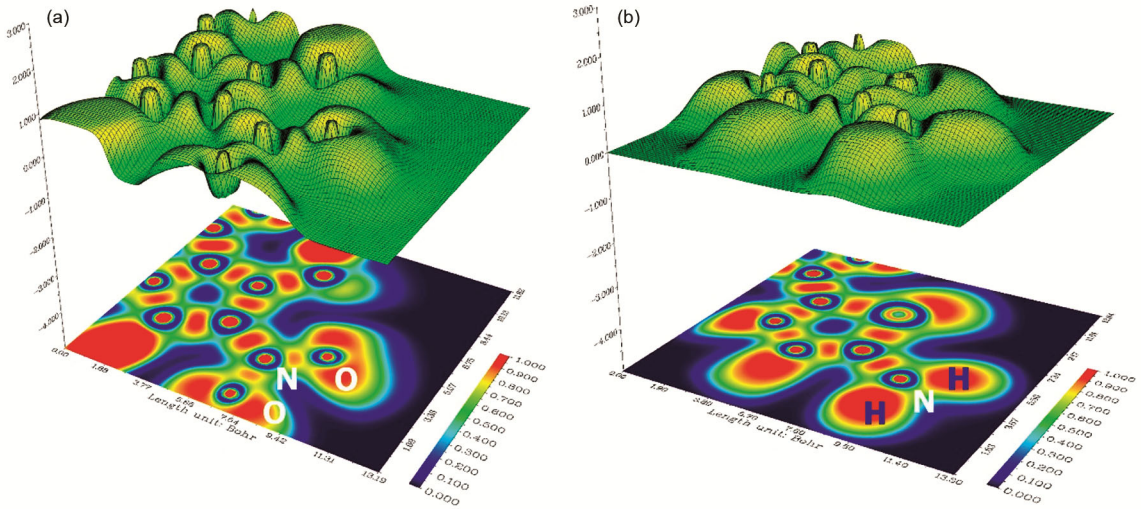

Fig. 7 — Shaded surface map for megazol

molecule's nucleus indicates the high electron depletion domains between its inner and valence shells. The five membered aromatic ring contains an electron depletion region in each atom. The highly localized electron zones are associated with the color red. The electron needs to be concentrated on the outside of the molecule in order to stabilize it.

Hole–electron transfer analysis

The tool used for electron excitation analysis is a massive computer software known as Multiwfn 3.8. This technique offers a comprehensive understanding of various types of electron transport characteristics and is particularly useful in displaying the properties of electron excitations[52]. The molecule under investigation consists of thiadiazole and imidazole rings as π-linkers, a nitro group (electron withdrawing) on the imidazole group, and an -NH_2 (electron donating) residue on the thiadiazole moiety. Since this specific molecule's electron excitation properties are being investigated, electron transfer is therefore possible.

Initially, the molecule is optimized using the same level of approach. After that, the CAM-B3LYP basis set is used to do the TD-DFT computation. The keyword IO*p*(9/40=4) is used. There is documentation for the fifteen lowest excited states. Different parameter values at the same theoretical level are shown in Table 7. Fig. 8 displays the different calculated characteristics alone for the lowest six excitations.

All the D index values are not large (below 2.0 Å). So all the excitations and can obviously, be considered local excitation (LE) only. For a charge transfer type of reaction, the D index may have a value above 2.0 Å. Additionally, Fig. 8 shows that for all six lowest excitations, there is a little space between the centeroids of the c_{hole}-c_{elec} centeroids, which are blue (holes) and green (electrons).

The Sr index values for each excited state are somewhat significant. They exhibit a n→π* transition to aromatic rings. The values need to be more than 0.8 a.u. in order for a π→π* transition to occur. The Sr index values for this investigation do not approach 0.8 a.u. Thus, only the lowest 15 excitations of these excitations exhibit a n → π* type transition.

The width of the typical spreading of holes and electrons is referred to as the H index. The hole-electron map (Fig. 8) shows that S0 → S1's holes and electrons are dispersed over the surrounding area. Its H index value (1.807 Å) is thus not very high. The higher dispersion of holes and electrons from S0 → S11, S15, and S10 leads to higher H index values (3.904, 3.523, and 3.272 Å, respectively). Since S0 through S6 have positive τ indices, there is a significant gap between the holes and electrons. It follows that the charge transfer (CT) kind of excitation is easily understood. The extraordinarily low hole-to-electron separation is confirmed by the tow indices, which are categorically negative for the remaining excitations from S0. They only react to local type (LE) stimulation as a result.

The transitions from S0 → S1, S3, S5, S8, S12, and S13 have low Δr values. Given their big Δr value, the other excitations could also have a significant CT

Table 7 — The HEI properties for megazol

S. No	Sm (a.u.)	Sr (a.u.)	D (Å)	H (Å)	τ (Å)	Excitation energy (eV)	Coulomb attractive energy (eV)	Δr (Å)	Λ
1	0.2627	0.5108	0.635	1.807	–0.641	3.938	8.0632	0.9962	0.4678
2	0.4333	0.7220	1.816	3.025	–0.923	3.954	5.3466	3.1807	0.6059
3	0.2854	0.5476	0.450	2.083	–1.213	4.434	7.4253	1.4666	0.4781
4	0.2588	0.5205	1.694	2.444	–0.055	4.763	5.7506	2.8951	0.4975
5	0.4714	0.7513	1.098	3.206	–1.709	4.862	5.1727	1.4947	0.6541
6	0.2057	0.4529	1.641	2.581	0.166	5.291	5.2720	3.6270	0.2892
7	0.4477	0.7393	1.571	2.967	–0.956	5.441	5.3001	2.7224	0.5448
8	0.2205	0.4708	1.449	2.568	–0.287	5.458	5.7013	1.0319	0.4725
9	0.3558	0.6753	1.827	2.880	–0.650	5.545	5.2931	2.5150	0.5392
10	0.3297	0.6046	1.498	3.272	–1.629	5.942	4.6805	2.5588	0.3709
11	0.4590	0.7346	0.881	3.904	–1.940	5.965	4.8465	2.2816	0.4903
12	0.2815	0.5599	1.136	2.802	–0.837	5.987	5.4034	1.4898	0.4801
13	0.4634	0.7639	1.087	2.584	–1.003	6.226	6.0697	1.9032	0.5947
14	0.3007	0.5803	0.651	2.614	–1.266	6.273	5.6427	3.0810	0.3077
15	0.2416	0.5144	0.290	3.523	–2.211	6.323	4.2054	2.3107	0.3052

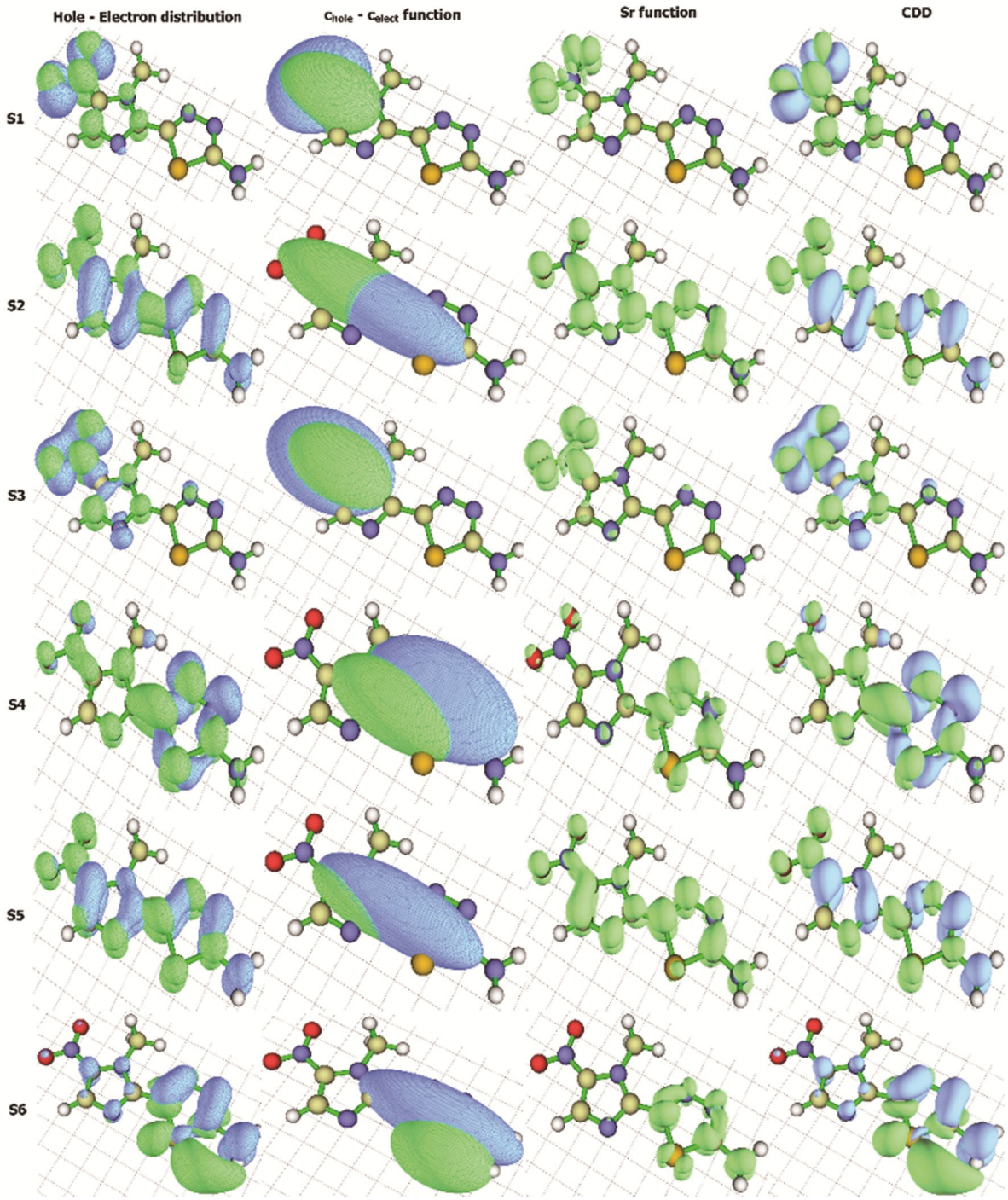

Fig. 8 — The Hole-electron distribution study pictorial representation of megazol (lowest six excitations only)

character. (According to the original article, the Δr value recommends employing 2.0 Å as a criterion to differentiate between excitations from LE and CT. S0 → S6 only follow CT excitation and have positive τ values, while other excitations adhere solely to LE type.

The values of Δr appear to be almost inversely related to the lambda (**Λ**). The hole-electron separation distance decreases with increasing hole-electron overlapping area. This is the obtained Λ value, 0.2892, for the shorter excited states, S0→S6. The following hypotheses have been

developed in view of the reports of the aforementioned iso-surface maps (Fig. 8) and Table 7:

S0→S1	LE (n-π*)	S0→S9	LE (n-π*)
S0→S2	LE (n-π*)	S0→S10	LE (n-π*)
S0→S3	LE (n-π*)	S0→S11	LE (n-π*)
S0→S4	LE (n-π*)	S0→S12	LE (n-π*)
S0→S5	LE (n-π*)	S0→S13	LE (n-π*)
S0→S6	CT (n-π*)	S0→S14	LE (n-π*)
S0→S7	LE (n-π*)	S0→S15	LE (n-π*)
S0→S8	LE (n-π*)		

IFCT interpretation

The inter-fragment charge transfer (IFCT) technique provides a means of quantifying the amount of CT across different segments for the S0 → S6 transition state. The same kinds of parameters that were employed in the computations mentioned before are also employed in this decision.

The thiadiazole ring of this molecule having an electron donor (-NH_2). is connected to the imdiazole moiety, which possesses a strong electron-withdrawing group (-NO_2). They can function as π-linkers because they have alternate double bonds in these five-membered ring structures. Fig. 9 shows the different fragment patterns.

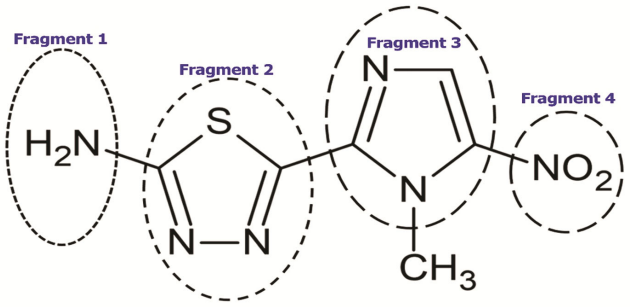

Fig. 9 — Pattern of fragmentation for IFCT scrutiny

Table 8 displays the findings obtained for the different fragments. Table 8's bottom section describes the transferred electrons (net amount) for the S0 → S6 excitation, while the top section shows the quantity of electrons that were transferred between the fragments. Additionally, the total amount of intra-fragment electron dispersion is reflected in the diagonal terms in the upper section.

Table 8 shows that for the S0 → S6 excitation, 0.2297 electrons are transferred from segment1 to segment 2, and that fragment 2 also donates 0.0812 electrons back to fragment 1 at the same time. Therefore, 0.1485 electrons are transferred net from fragment 1 to fragment 2. Meanwhile, fragment 1 sends 0.0018 electrons to fragment 3 and 0.0040 electrons to fragment 4. Thus, we may conclude with confidence that 0.0019 electrons are removed from NH_2 (Fragment 1), by NO_2 (Fragment 6), *via* the π-linkers. Hence, charge transfers are possible. Since the sulphur atom being an electron-withdrawing group, it takes 0.0959 electrons from fragment 3, hence a negative sign is mentioned.

Heat map investigations

In order to see nature in its lowest six excitation levels, heat maps are created. The same pattern of four fragments is considered for the determinations (Fig. 9). Table 9 displays the computed percentages of hole, electron, overlap, and difference. Fig. 10 shows the heat maps that were produced.

From Table 9 and Fig. 10, the following observations are made: Only the nitro group is abundant in holes and electrons in the S0 → S1 excitation. In the S0 → S2 excitation, the quantity of hole is more in fragment 3 (imidazole). The S0 → S3 excitation has almost the same nature as the S0 → S1 excitation. The fragment 2 (thiadiazole) has a high

Table 8 — Net transferred and transferred electrons details between fragments

	Fragment 1 (NH_2)	Fragment 2 (thiadiazole)	Fragment 3 (imidazole)	Fragment 4 (NO_2)
	Transferred electrons between fragments (diagonal terms corresponds to amount of intra-fragment electron redistribution)			
Fragment 1 (NH_2)	0.0390	0.2297	0.0018	0.0040
Fragment 2 (thiadiazole)	0.0812	0.4779	0.0037	0.0084
Fragment 3 (imidazole)	0.0169	0.0996	0.0007	0.0018
Fragment 4 (NO_2)	0.0022	0.0128	0.0001	0.0002
	Net transferred electrons between fragments			
Fragment 1 (NH_2)	---	0.1485	–0.0151	0.0019
Fragment 2 (thiadiazole)	---	---	–0.0959	–0.0044
Fragment 3 (imidazole)	---	---	---	0.0017
Fragment 4 (NO_2)	---	---	---	---

amount of holes in the S0 → S4 excitation state. In the case of the S0 → S5, the fragment 3 is richer in holes whereas fragment 2 is richer in electrons. The electron is richer in fragment 2 in the S0 → S6 excitation state.

Table 9 — The various parameters in percentage for megazol

Excitation	Fragment	Hole (%)	Electron (%)	Overlap (%)	Difference (%)
S1	1 (NH_2)	0.13	0.52	0.26	0.39
	2 (thiadiazole)	0.45	1.64	0.86	1.19
	3 (imidazole)	6.25	15.41	9.81	9.16
	4 (NO_2)	93.50	82.83	88.00	–10.67
S2	1 (NH_2)	14.72	5.30	8.83	–9.41
	2 (thiadiazole)	35.22	28.70	31.79	–6.52
	3 (imidazole)	61.74	28.09	41.64	–33.65
	4 (NO_2)	14.95	52.15	27.93	37.19
S3	1 (NH_2)	–0.00	0.52	0.00	0.52
	2 (thiadiazole)	3.76	4.79	4.24	1.03
	3 (imidazole)	13.45	17.00	15.12	3.55
	4 (NO_2)	84.29	79.89	82.06	–4.40
S4	1 (NH_2)	4.75	12.50	7.70	7.76
	2 (thiadiazole)	102.67	73.93	87.12	–28.73
	3 (imidazole)	33.10	22.26	27.15	–10.84
	4 (NO_2)	8.64	32.04	16.69	23.34
S5	1 (NH_2)	18.86	12.21	15.17	–6.65
	2 (thiadiazole)	41.72	52.65	46.87	10.92
	3 (imidazole)	57.21	25.76	38.39	–31.45
	4 (NO_2)	14.13	41.79	24.30	27.66
S6	1 (NH_2)	38.56	–24.42	0.00	–62.98
	2 (thiadiazole)	61.97	163.89	100.78	101.92
	3 (imidazole)	30.77	12.01	19.93	–17.87
	4 (NO_2)	16.13	37.58	24.62	21.45

STM study

The Multiwfn 3.8 program is used to create a simulated scanning tunneling microscope (STM) image. An effective instrument for explaining the material surface and adsorbates is a scanning tunneling microscope[53]. To create STM pictures of exfoliable 2D materials, DFT is utilized[54]. Using a conceptual version of an s-wave STM tip, the Tersoff-Hamann technique is used to compute the STM pictures[55].

$$n(r,E) = \sum_{\mu} \left|\psi_{\mu}(r)\right|^2 \delta(\varepsilon_{\mu} - E) \quad \ldots(11)$$

$$I(r,V) \propto \int_{E_F}^{E_F+eV} dE\, n(r,E) \quad \ldots(12)$$

In this computation, the applied voltage (V) and tip location (r) determine the tunneling current (I). The integrated local density of states (ILDOS) determines its proportionality. The Kohn-Sham eigenvectors ψ_{μ}, and eigenvalues, ε_{μ}, where μ designates distinct states, are used to compute the ILDOS value. EF stands for Fermi energy.

Plotting of the obtained pictures at (a) V = -3.5 V at Z = 2.2 Å and (b) V = -3.5 V at Z = 0.5 Å conditions is shown in Fig. 11. The Tersoff-Hamann model suggests a positive correlation between tunneling current and LDOS, with brighter white maps indicating greater LDOS and larger tunneling current (I). In this current investigation, when the situation is changed (V = -3.5 V at Z = 0.5 Å), the tunneling

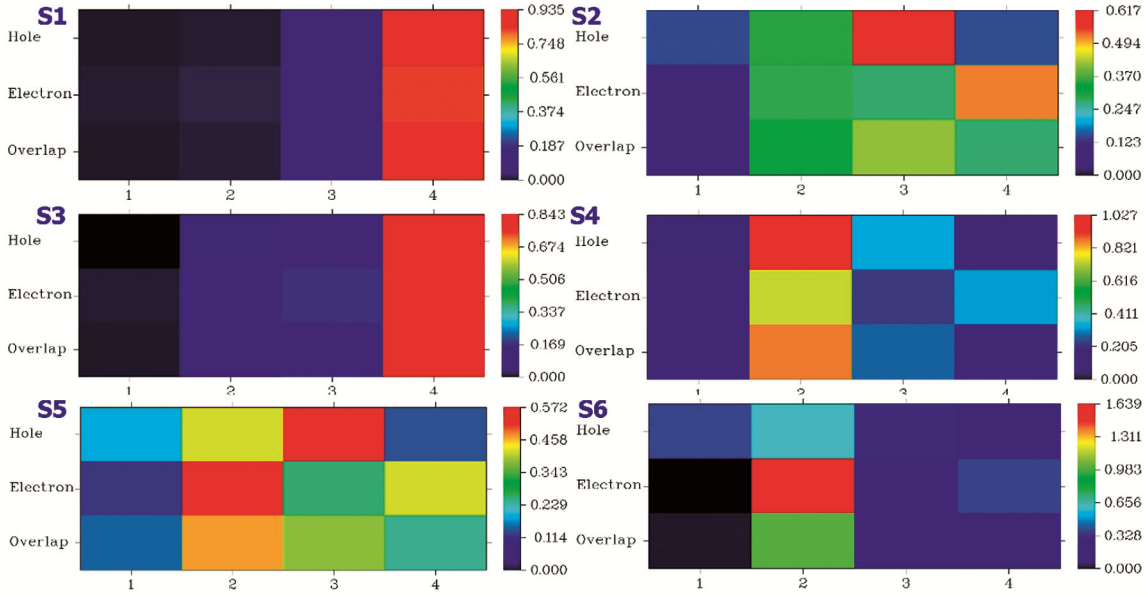

Fig. 10 — Heat maps generated for megazol

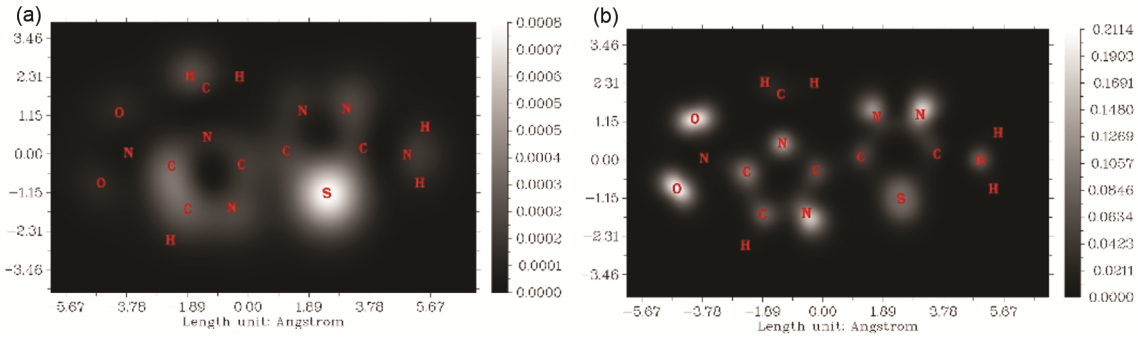

Fig. 11 — The simulated STM images for megazol

Table 10 — Thermodynamic properties at different temperatures for megazol

Temperature (K)	S (cal/mol/K)	CV (cal/mol/K)	CP (cal/mol/K)
100	78.682	21.314	23.301
200	96.998	35.805	37.792
300	113.345	48.885	50.872
400	128.507	60.365	62.352
500	142.632	69.911	71.899
600	155.744	77.562	79.550
700	167.888	83.650	85.637
800	179.140	88.538	90.525
900	189.585	92.521	94.508
1000	199.311	95.813	97.800

current is firmly positioned on the two oxygen atoms of the nitro group and highly located on the sulfur atom in the first instance (V = -3.5 V at Z = 2.2 Å). Additionally, in comparison to the first scenario, the later one shows a clearer distribution of the tunneling current on the ring system.

Effect of temperature on S, CV, and CP for the title molecule

To determine how temperature affects entropy (S), specific heat at constant volume (CV), and specific heat at constant pressure (CP) for the molecule under study, the frequency computations from the Shermo software are utilized. Table 10 displays the results from 100 K to 1000 K, and Fig. 12 plots a graph of those results.

Table 10 and Fig. 11 prove how these thermodynamic functions (S, CV and CP) rise with temperatures between 100 and 1000 K. The polynomial equations are:

$S\ (y) = 56.8202 + 0.2154\ T - 3.9720\ e^{-5}\ T^2$ ($R^2 = 0.9999$)

$CV\ (y) = 5.998 + 0.1647\ T - 7.573\ e^{-5}\ T^2$ ($R^2 = 0.9994$)

$CP\ (y) = -1.5554 + 0.1647\ T - 7.574\ e^{-5}\ T^2$ ($R^2 = 0.9994$)

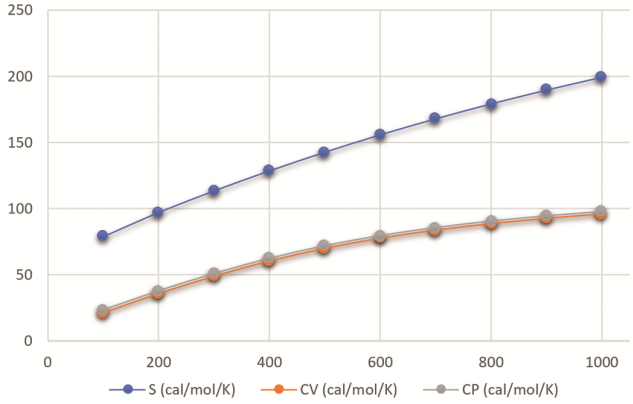

Fig. 12 — Effect of temperature CP, CV and S for megazol

Theoretical UV-Vis analysis

TD-DFT calculations have predicted electronic transitions, energies, wavelengths, absorption spectra and oscillator strengths at the same theoretical level. The ethanol solvent is used for the computations. For the computation, the IEFPCM solvation model is recommended. The simulated UV-Vis spectra for various solvents are displayed in Fig. 13. Table 11 lists the principal contributions of the transitions together with the absorption wavelengths (λ), oscillator strengths (f), and excitation energies (E) for the ethanol solvent.

We can see from Fig. 13 that the absorption occurs about between 325 and 465 nm. Three sharp electronic transitions at wavelengths of 361.6, 328.9, and 303.7 nm are predicted. The highest oscillator strength (0.4024) is observed at 361.6 nm. The peak at 361.6 nm (energy = 27651.11 cm^{-1}) is developed from the electronic excitation of HOMO → LUMO (99%). HOMO is observed at the 58th orbital. The peak at 328.9 nm (energy = 30395.81 cm^{-1}) is due to the large contributions of HOMO-5→ LUMO (14%), HOMO-3→LUMO (66%), HOMO-1→LUMO (14%), and the tiny contribution of HOMO-3→ LUMO +1 (4%). The major contributions

of HOMO-5→LUMO (14%), HOMO-3 → LUMO (66%), and the minor contributions of HOMO-8→LUMO (5%), and HOMO-3→LUMO (5%), HOMO-1→LUMO+1 (5%) are the main cause for the growth of a peak at 303.7 nm (energy = 32922.75 cm^{-1}). The theoretical UV spectra of benzene, chloroform, diethyl ether, DMSO, ethanol, methanol, and water are recorded and presented in Fig. 13.

Computed vibrational frequency analysis

Vibrational spectroscopy measures the interaction of infrared light with matter to determine the chemical nature and functional groups of substances. With 21 atoms dispersed over many planes, the target molecule vibrates in 57 group vibrational modes and finger-print vibrations. With 21 atoms, the title molecule may vibrate in 57 different normal modes. Forty of the 57 typical vibration modes are in-plane, while the other 17 are out-of-plane. The molecule's in-plane bands are denoted by A′ and its out-of-plane bands by A″. Thus, the title molecule's 57 normal modes of vibration are distributed as Γ_{Vib} = 40 A′ + 17 A″. The simulated vibrations were calculated using the same basis set and presented in Table 12. The theoretical values are also compared with the computed values using the 6-311G(d,p) basis set, and it was found that there is considerable agreement (Fig. 14). The generated IR spectrum is plotted in Fig. 15.

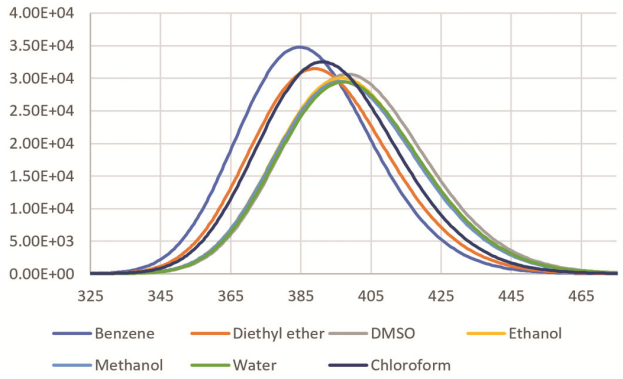

Fig. 13 — The theoretical UV-Vis spectrum in several solvents for megazol

Vibrational analysis

(a) NH_2 vibrations

The vibrational frequencies for the amino group[1,2] present in megazol, the asymmetric stretching vibrations, were observed at 3566 cm^{-1} as a medium intensity band. The symmetric stretching was observed at 3454 cm^{-1} as a strong, intense peak. The scissoring vibrations appeared at 1586 cm^{-1}.

(b) N=O vibrations

The nitro group[2,3] vibration shows its prominence between 1514, 1134, and 1259 cm^{-1} for stretching vibrations as a strong, intense peak. Further, a very weak peak appeared at 575, 420, and 355 cm^{-1}. At 815 cm^{-1} a medium-intensity peak was noted due to the nitro group. They show at 1682 and 1673 cm^{-1} in the simulated spectra. It's interesting to note that the experimental value is likewise determined to be precisely located as a single strong peak at 1673 cm^{-1}.

(c) C=N vibrations

Within the range of 1586–1120 cm^{-1}, the complete stretching vibrations of C–C=N and C=N–C were detected[3,8]. The C=N stretching vibrations in this fascinating molecule were found at 1586, 1521, 1514, 1470, 1461, and 1453 cm^{-1}. The C=N stretching vibrations were also identified as having very weak, medium-to-strong peaks at 1392, 1376, 1345, 1313, 1294, 1259, 1189, 1150, 1130, and 1120 cm^{-1}.

(d) CH_3 vibrations

Asymmetric stretching of the methyl carbon bonded to the nitrogen nucleus results in the appearance of a very faint peak between 3077 and 3042 cm^{-1}. The symmetric vibration was observed at 2972 cm^{-1} with a very weak intensity.

Table 11 — Theoretical UV-Vis parameters and electronic transitions in ethanol of megazol

Calculated wavelength (nm)	Energy (cm^{-1})	Osc. Strength (f)	Major contributions	Minor contributions
361.6	27651.11	0.4024	HOMO →LUMO (99)	---
328.9	30395.81	0.0001	HOMO-5→LUMO (14%), HOMO -3→LUMO (66%), HOMO -1→LUMO (14%)	HOMO -3→ LUMO +1 (4%)
303.7	32922.75	0.0011	HOMO -5→LUMO (12%), HOMO -1→LUMO (69%)	HOMO-8→LUMO (5%), HOMO -3→LUMO (5%), HOMO -1→LUMO+1 (5%)

Table 12 — Theoretical vibrational analysis for megazol and the assignments of vibrations with PED by 6-311G(d,p) and 6-311++G(d,p) basis sets

S. No	S[y]	6-311G(d,p)		6-311++G(d,p)		Strength of signal	Assignments with PED (%)
		Unscaled	Scaled (0.9642)	Unscaled	Scaled (0.9662)		
1	A′	3688	3556	3691	3566	m	ν_aNH_2 (66), $\nu_a NH_2$ (34)
2	A′	3573	3445	3575	3454	s	ν_sNH_2 (34), ν_sNH_2 (66)
3	A′	3268	3151	3267	3156	vw	νCH_{aro} (99)
4	A′	3185	3071	3185	3077	vw	ν_aCH_{met} (11), ν_aCH_{met} (79)
5	A′	3149	3036	3149	3042	vw	ν_aCH_{met} (79)
6	A′	3076	2966	3076	2972	vw	ν_sCH_{met} (39), ν_sCH_{met} (39) ν_sCH_{met} (21)
7	A′	1645	1586	1642	1586	vs	σNH_2 (79), νNC_{aro} (10)
8	A′	1592	1535	1575	1521	m	νCC_{aro} (26), νNC_{aro} (21)
9	A′	1578	1521	1567	1514	vs	νON_{aro} (31), νON_{aro} (28) νNC_{aro} (10)
10	A′	1526	1472	1521	1470	vw	νNC_{aro} (17), νCC_{aro} (18) νNC_{aro} (13)
11	A′	1518	1464	1512	1461	vs	νCC_{aro} (10), νNC_{aro} (24)
12	A′	1506	1452	1504	1453	vs	σHCH_{met} (40), νNC_{aro} (12)
13	A′	1504	1450	1502	1451	vw	σHCH_{met} (36), σHCH_{met} (38)
14	A′	1503	1449	1499	1449	m	σHCH_{met} (20), σHCH_{met} (16), νCC_{aro} (18)
15	A′	1443	1391	1441	1392	vw	ωHCH_{met} (17), νNC_{aro} (14)
16	A′	1428	1377	1425	1376	m	μNCN_{aro} (21), νCC_{aro} (13) νNC_{aro} (30)
17	A′	1396	1346	1392	1345	vs	νNC_{aro} (13), νNC_{aro} (32) νON_{nit} (19), νON_{nit} (15)
18	A′	1365	1316	1359	1313	vs	μCCN_{aro} (18), νNC_{aro} (14) νNC_{aro} (29)
19	A′	1343	1295	1340	1294	vw	μNCN_{aro} (15), μHNC_{aro} (27), νNC_{aro} (20)
20	A′	1308	1261	1304	1259	vs	μNCN_{aro} (11), νNC_{aro} (29) νON_{nit} (14), νON_{nit} (18)
21	A′	1234	1190	1231	1189	vs	νNC_{aro} (19), νNC_{aro} (18)
22	A′	1190	1147	1190	1150	vw	νNC_{aro} (10)
23	A′	1172	1130	1170	1130	vs	νNN_{aro} (50), νNC_{aro} (12)
24	A′	1160	1119	1160	1120	vw	νNC_{aro} (13)
25	A′	1156	1115	1153	1114	vw	ρHCH (16), ρHCH (16)
26	A′	1065	1026	1060	1024	vw	μCCN (14), μHNC (46) νNN (22), νNC (16)
27	A′	1038	1001	1038	1003	w	μNNC (31), μNCN (10) νNC (15)
28	A′	935	902	934	903	vw	μNNC (11), μCNC (44) μCCN (11), μNCN (10)
29	A″	898	865	891	861	vw	βCCNC (10), βHCNC (87)
30	A′	847	817	843	815	m	μCCN (11), μONO (57)
31	A′	784	756	783	757	vw	μSCN (11), μCNN (51)
32	A″	747	721	733	708	vw	δCNNC (28), δOCON (11) δCNCN (43)
33	A″	737	711	719	695	vw	δOCON (78)

(*Contd*.)

Table 12 — Theoretical vibrational analysis for megazol and the assignments of vibrations with PED by 6-311G(d,p) and 6-311++G(d,p) basis sets

S. No	S^y	6-311G(d,p)		6-311++G(d,p)		Strength of signal	Assignments with PED (%)
		Unscaled	Scaled (0.9642)	Unscaled	Scaled (0.9662)		
34	A′	710	684	707	683	vw	μNCN (12), νNC (42) νNC (11)
35	A′	658	634	661	639	vw	νSC (77)
36	A′	636	613	632	611	vw	βSCN (29)
37	A″	624	602	621	600	vw	δNSNC (42), τSCNN (20)
38	A″	613	591	604	584	vw	τCCNC (62), τCNNC (11)
39	A′	596	575	595	575	vw	μSCN (16), μCNC (12) μONC (12)
40	A″	581	560	577	558	vw	τCNNC (69)
41	A″	495	477	481	464	vs	τHNCS (36), νNC (12)
42	A″	474	457	471	455	vs	ωHNCS (29), νNC (16)
43	A′	435	419	434	420	vw	μSCN (11), μNCN (12) μONC (24), μNCC (13)
44	A″	400	385	393	380	w	δCNNC (11), δNSNC (16) τNNCC (30), τCNCN (12)
45	A′	367	354	367	355	vw	μCNC (28), μNCN (37) μONC (10)
46	A′	328	316	326	315	vw	μCNC (26), μNCN (12) μCCN (15)
47	A″	310	298	309	298	m	μHNCS (15), μHNCS (36)
48	A′	274	264	273	264	vw	μNCC (18), νCC (20)
49	A″	252	243	246	238	vw	δCNNC (19), δNSNC (12) τSCNN (27)
50	A″	237	228	231	223	vw	δCCCN (38), δNNCC (35) τHCNC (14), βONC (14)
51	A′	214	206	213	205	vw	μNCC (40), μNCC (11)
52	A″	165	159	154	149	vw	δCCCN (33), τHCNC (24) τHCNC (24), τHCNC (12)
53	A″	131	127	128	123	vw	δNNCC (16), τSCNN (20) τNNCC (26)
54	A′	105	102	105	101	vw	μNCC (41), μCCN (37)
55	A″	60	58	54	52	vw	δCNNC (27), δNNCC (18) τNNCC (25), τCNCN (11)
56	A″	54	52	48	47	vw	τONCN (72)
57	A″	43	42	38	36	vw	τNCCN (83)

S^y, symmetry; ν, stretching; $ν_s$, sym. stretching; $ν_a$, asym. stretching; σ, scissoring; τ, torsion; ω, wagging; ρ, rocking; δ out; μ; in-plane bending; β, out-plane bending; aro, aromatic; met, methyl; nit, nitro.

(e) N-N vibrations

The NN stretching vibrations[3,8,11] appeared as a very weak band at 1024 cm^{-1}, and the aromatic NN stretching band appeared at 1130 cm^{-1}. The CNNC vibrations appeared with a very weak to weak band between 708 and 52 cm^{-1}.

(f) SCN vibrations

The sulphur atom attached to carbon and nitrogen simultaneously appeared as a very weak band between 757 and 420 cm^{-1}. The SCNN vibrations emerged as weak torsional vibrations between 600, 238, and 123 cm^{-1}.

Toxicity analysis

Megazol is an anti-Chagas' disease dr0075g that has been found to have cytotoxic and genotoxic effects[56]. Studies have shown that the drug can cause DNA damage in bacteria and can be toxic to cells that are defective in DNA repair[57]. Due to its toxicity, it is

not recommended for further development for the treatment of Chagas' disease[56].

The toxicity of megazol is analyzed *in-silico* using the EPA DSS TOX[58] and given in Table 13. LC_{50}

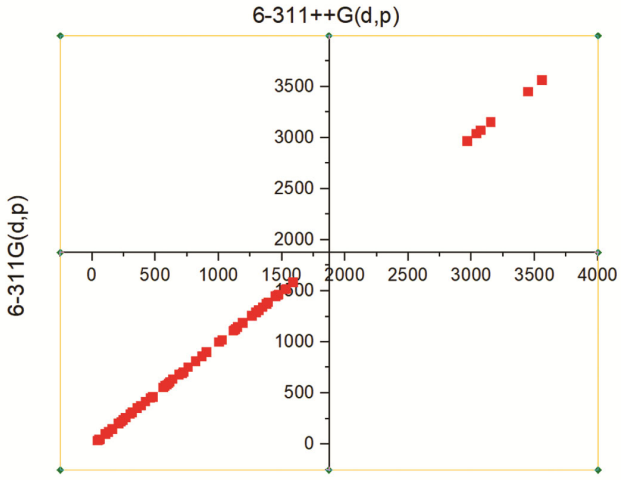

Fig. 14 — The comparison of IR data obtained by 6-311G(d,p) and 6-311++G(d,p) basis sets for megazol

analyses were carried out *in-silico* in *Daphnia Magna* for 48 hours. The results showed that the values for LC_{50} in *Daphnia Magna* at 48 hours fell between 3.28 – Log_{10} (mol/L) and 117.332 mg/L. The hierarchical clustering falls between 2.739 – Log_{10} (mol/L) and the nearest neighbour method of analysis with 38.041 mg/L and 3.774 – Log_{10} (mol/L) and group consensus with 117.554 mg/L and 3.284 – Log_{10} (mol/L) subjectively[59].

The oral LD_{50} analysis of the *Mus musculus* model showed that the title compound is less toxic to mammals. Having been with 2.123 – Log_{10} (mol/kg) to 1704.467 mg/kg nearest neighbour analysis (NNA), which showed that the toxicity level is too low or negligible to be considered. In the literature, Megazol has been found to be highly toxic and can cause reactive encephalopathy in 5-10% of treated patients, of which 50% can be fatal[60].

The recommended dosage of megazol varies depending on the condition being treated. For example, in the treatment of Chagas' disease, a study

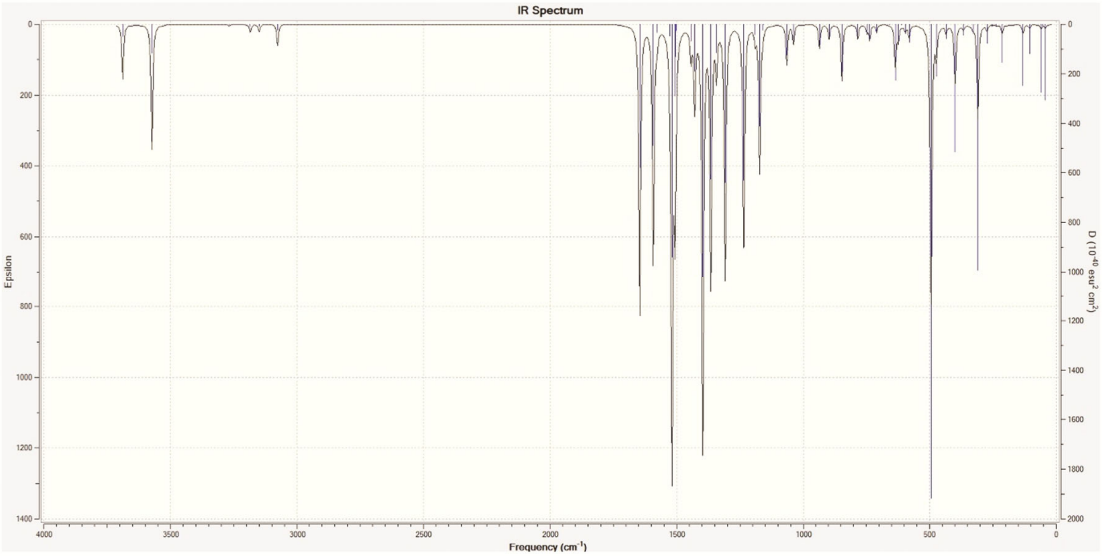

Fig. 15 — Theoretical IR spectrum calculated for megazol at B3LYP/6-311++ G(d,p) level

Table 13 — Toxicity information as revealed through EPA DSS TOX for megazol

S. No	Property	Consensus	Hierarchical clustering	Single model	Group contribution	Nearest neighbor
1	48 hour D. magna LC_{50}	3.285 -Log_{10}(mol/L) 117.332 mg/L	3.343 -Log_{10}(mol/L) 102.814 mg/L	2.739 -Log_{10}(mol/L) 412.209 mg/L	3.284 -Log_{10}(mol/L) 117.554 mg/L	3.774 -Log_{10}(mol/L) 38.041 mg/L
2	Oral rat LD_{50}					2.123 -Log_{10}(mol/kg) 1704.467 mg/kg
3	Bioconcentration factor	0.253 Log_{10} 1.790	0.460 Log_{10} 2.881	0.014 Log_{10} 1.033	0.285 Log_{10} 1.927	
4	Developmental toxicity	True	True	False		True
5	Ames mutagenicity	True	True			True
6	Estrogen Receptor Binding	False	False	False		

in Swiss mice found that a dosage of 20 mg/kg administered intraperitoneally (i.p.) cured the infection, while a dosage of 80 mg/kg administered orally also resulted in a cure[21]. Another study in mice used a combination treatment of 20 mg/kg of suramin administered i.p., followed by 4 daily doses of 80 mg/kg of megazol given either i.p. or oral[61]. In a different study, the treatment consisted of 20 mg/kg of suramin administered i.p. alone or three daily doses of 80 mg/kg of megazol[62].

The developmental toxicity is true in most cases for the title compound, but bearing in mind that the single model sometimes validates it as false. Regarding its Ames mutagenicity, the values were true for all the *in silico* analyses. This compound has no potential to bind with the estrogen receptor, so it may not have the tendency to show reproductive toxicity.

The *in silico* prediction using the pkCSM server for toxicity analysis confirms the AMES toxicity, Hepatotoxicity, Oral Rate Acute Toxicity LD_{50} (1.931 mol/kg), Oral Rat Chronic Toxicity (LOAEL) (1.704 log mg/kg_bw/day), *T.Pyriformis* toxicity (0.285 log ug/L), Minnow toxicity (1.334 log mM), and so on. However, it showed negative results for skin sensitization, hERG I, II inhibitor, CYP3A4 inhibitior, P-glycoprotein II inhibitor, *etc*.[63]

On a cumulative analysis, the title compound could be considered less toxic. However, it could be toxic for lower organisms, and for most higher organisms, like mammals, it may have low toxicity[64]. It's important to note that the recommended dosage and duration of treatment with megazol should be determined by a healthcare professional based on the specific condition being treated. The information provided here is based on an *in silico* analysis using animal models, and the dosage for human use may differ. It is crucial to consult a doctor or healthcare provider for the appropriate use of this medication.

Conclusion

Megazol is a wonderful drug molecule that is used to treat acid-related diseases of the stomach. The electronic structures and other attributes are found using the DFT/B3LYP/6-311++G(d,p) level of theory. ESP analysis predicts that there are electron rich and poor sites available in the molecule. FMO analysis communicates that this is a stable and hard molecule. According to NBO determination, this is a stable molecule. According to NPA analysis, the molecule is more vulnerable to nucleophilic assault at 13N, which is explained by the Fukui function. The NCI determination reveals that this molecule has van der Waals (vdW) forces and steric factors in it. The molecule's electron-rich and electron-poor domains are explained by a shaded surface map that projects the LOL determination. Hole-electron transfer experiment proves that charge transfer is possible at S6 excitation only. The local excitation (LE) is followed by all subsequent excitations. Electrons are moving across the π-linkers from $-NH_2$ (electron donor) to $-NO_2$ (electron acceptor), as explained by the intra-fragment transfer study. Heat maps are discussed for the lowest six excitations. The tunneling current spreads across the ring when V = - 3.5 V at Z = 0.5 Å, as explained by the STM study. The thermodynamic parameters S, CV, and CP increase when the temperature is increased. Simulated UV-Vis spectral analysis explains that three peaks are developed. Simulated IR frequencies are discussed. The toxicity of the molecule is explained.

Acknowledgement

The authors are thankful to the Principal of St. John’s College, Palayamkottai, for providing the computer and software facilities.

Funding

Funding organizations from the governmental, private, or nonprofit sectors did not provide any special grants for this study.

Declaration of competing interest

The authors declare that they have no known competing financial interests or personal relationships that could have appeared to influence the work reported in this paper.

References

1 Li Z Z, V Li, Tangadanchu K R, Battini N, Bheemanaboina R R Y, Zang Z L, Zhang S L & Zhou C H, *Eur J Med Chem,* 179 (2019) 723.
2 Günay N S, Çapan G, Ulusoy N, Ergenç N, Ötük G & Kaya D, *Il Farmaco,* 54 (1999) 826.
3 Varshney V, Mishra N N, Shukla P K & Sahu D P, *Eur J Med Chem,* 45 (2010) 661.
4 Liu K & Zhu H L, *Anti-Cancer Agents Med Chem,* 11 (2011) 687.
5 Fung H B & Doan T L, *Clin Ther,* 27 (2005) 1859.
6 Silvestri R, Artico M, De Martino G, Ragno R, Massa S, Loddo R, Murgioni C, Loi A G, La Colla P & Pani A, *J Med Chem,* 45 (2002) 1567.
7 Al-Soud Y A, Al-Masoudi N A, Hassan H G H, De Clercq E & Pannecouque C, *Acta Pharm,* 57 (2007) 379.
8 Poorrajab F, Ardestani S K, Emami S, Behrouzi-Fardmoghadam M, Shafiee A & Foroumadi A, *Eur J Med Chem,* 44 (2009) 1758.

9 Gardner T B, & Hill D R, *Clinic Microbio Rev*, 14 (2001) 114.
10 Riches A, Hart C J S, Trenholme K R, & Skinner-Adams T S, *J Med Chem,* 63 (2020) 13320.
11 Olender D, Żwawiak J, Lukianchuk V, Lesyk R, Kropacz A, Fojutowski & Zaprutko L A, *Eur J Med Chem,* 44 (2009) 645.
12 Lau H, Lam N P, Piscitelli S C, Wilkes L, Danziger L H, *Clin Pharm,* 23 (1992) 328.
13 Tukulula M, Sharma R K, Meurillon M, Mahajan A, Naran K, Warner D, Huang J, Mekonnen B & Chibale K, *ACS Med Chem Lett*, 4 (2013) 128.
14 Mukherjee T & Boshoff H, *Future Med Chem*, 3 (2011) 1427.
15 Ang C W, Jarrad A M, Cooper M A & Blaskovich M A, *J Med Chem*, 60 (2017) 7636.
16 Shalini, Viljoen A, Kremer L, & Kumar V, *Bioorg Med Chem Lett,* 28 (2018) 1309.
17 Stover C K, Warrener P, Van Devanter D R, Sherman D R, Arain T M, Langhorne M H, Anderson S W, Towell J A, Yuan Y & McMurray D N, *Nature*, 405 (2000) 962.
18 De Castro S L, *Acta Trop,* 53, (1993) 83.
19 Chapman J D, Lee J, & Meeker B E, *Int J Radiat Oncol Biol Phys,* 16 (1989) 911.
20 Bouteille B, Marie-Daragon A, Chauvière G, Albuquerque C, Enanga B, Darde M L, Vallat J M, Périé J, & Dumas M, *Acta Trop* 60 (1995) 73.
21 Filardi L S, & Brener Z, *Ann Trop Med Parasitol,* 76 (1982) 293.
22 Ferreira R C C & Ferreira L C S, *Mutat Res,* 171 (1986) 11.
23 De Morais M A, Ferreira R C C & Ferreira L C S, *Genet Mol Biol,* 21 (1998) 567.
24 Mital A, *Sci Pharm,* 77(3) (2009) 497.
25 Wang C, *Annu Rev Pharm Toxicol*, 35 (1995) 93.
26 Sjordsma & Schechter P J, *Clin Pharm Ther*, 35 (1984) 287.
27 Jeelani, Muthua S & Narayana B, *J Mol Struc*, 1241 (2021) 130558.
28 ACD/Labs | Software for R&D | Chemistry Software," ACD/Labs, (n.d.). https://www.acdlabs.com.
29 Hanwell M D, Curtis D E, Lonie D C, Vandermeersch T, Zurek E & Hutchison G R, *J Cheminformatics,* 4 (2012) 17.
30 Becke D, *J Chem Phys*, 98 (1993) 5648.
31 *Gaussian 16, Revision C01*, Frisch M J, Trucks G W, Schlegel H B, Scuseria G E, Robb M A, Cheeseman J R, Scalmani G, Barone V, Petersson G A, Nakatsuji H, Li X, Caricato M, Marenich A V, Bloino J, Janesko B G, Gomperts R, Mennucci B, Hratchian H P, Ortiz J V, Izmaylov A F, Sonnenberg J L, Williams-Young D, Ding F, Lipparini F, Egidi F, Goings J, Peng B, Petrone A, Henderson T, Ranasinghe D, Zakrzewski V G, Gao J, Rega N, Zheng G, Liang W, Hada M, Ehara M, Toyota K, Fukuda R, Hasegawa J, Ishida M, Nakajima T, Honda Y, Kitao O, Nakai H, Vreven T, Throssell K, Montgomery J A, Jr Peralta J E, Ogliaro F, Bearpark M J, Heyd J J, Brothers E N, Kudin K N, Staroverov V N, Keith T A, Kobayashi R, Normand J, Raghavachari K, Rendell A P, Burant J C, Iyengar S S, Tomasi J, Cossi M, Millam J M, Klene M, Adamo C, Cammi R, Ochterski J W, Martin R L, Morokuma K, Farkas O, Foresman J B & Fox D J, (Gaussian, Inc, Wallingford CT), 2016.
32 Schlegel H B, *J Comp Chem*, 3 (1982) 214.
33 O'Boyle N M, Tenderholt A L, & Langner K M, *J Comp Chem*, 29 (2008) 839.
34 Jamroz M H, *Spectrochim Acta A Mol Biomol Spect,* 114 (2013) 220.
35 Lu T & Chen F, *J Comp Chem,* 33 (2012) 580.
36 Humphrey W, Dalke A & Schulten K, *J Mol Graph*, 14(1) (1996) 33.
37 Lu T & Chen Q, *Comp Theor Chem,* 1200 (2021) 113249.
38 Jeyavijayan S, & Murugan P, *Asian J Chem*, 32 (2020) 83.
39 Er M, Isildak G, Tahtaci H, & Karakurt T, *J Mole Struc*, 1110 (2016) 102.
40 Politzer P & Murray J S, *Theor Chimi Acta,* 108 (2002) 134.
41 Saravanan S & Balachandran V, *Spectrochim Acta Part A: Mol Biomol Spec*, 138 (2015) 406.
42 Saraçoğlu H, Doğan O E, Ağar T, Dege N & Iskenderov T S, *Acta Cryst E Cryst Comm*, 76 (2020) 141.
43 Kores J J, Danish I A, Sasitha T, Stuart J G, Pushpam E J & Jebaraj W, *Heliyon*, 7 (2021) e08377.
44 Li L, Wu C J, Wang Z, Zhao L, Li Z, Sun C & Sun T, *Spectrochim Acta A Mol Biomol Spect*, 5 (2015) 338.
45 Li J N, Chen Z R & Yang S F, *Zhejiang Univ Sci*, 6B (2005) 584.
46 Kavitha E, Sundaraganesan N, Sebastian S & Kurt M, *Spectrochim Acta Part A Mol Biomol Spect*, 77 (2010) 612.
47 Parr R G & Yang W, *J Am Chem Soc,* 106 (1984) 4049.
48 Zacharias O, Varghese A, Akshaya K B, Savitha M S & George L, *J Mol Struc*, 1158 (2018) 1.
49 Morell, Grand A & Toro-Labbé A, *J Phys Chem* A, 109 (2005) 205.
50 Bandyopadhyay P, Karmakar A, Deb J, Sarkar U & Md Seikh M, *Spectrachim Acta Part A*, 228 (2019) 117827.
51 Schmider H L & Becke A D, *J Mol Struc Theo Chem*, 527 (2000) 51.
52 Liu Z, Lu T & Chen Q, *Carbon,* 165 (2020) 461.
53 Choudhary K, Garrity K F, Camp C, Kalinin S V, Vasudevan R, Ziatdinov M & Tavazza F, *Sci Data,* 8 (2021) 57.
54 Binnig G, Rohrer H, Ch Gerber & Weibel E, *Phys Rev Lett*, 49 (1982) 57
55 Tersoff J & Hamann D R, *Phys Rev B*, 31 (1985) 805.
56 Poli P, Mello M A D, Buschini A, Mortara R A, Albuquerque C N D, Silva S D, Rossi C & Zucchi T M A D, 64 (2002) 1617.
57 Enanga, Ariyanayagam M R, Stewart M L & Barrett M P, *Antimicro Agents Chemo*, 47 (2003) 3368.
58 Distributed Structure-Searchable Toxicity (DSSTox) Database | US EPA," US EPA, www.epa.gov, 14 Sept (2015) https://www.epa.gov/chemical-research/distributed-structure-searchable-toxicity-dsstox-database.
59 Chauvière G, Bouteille B, Enanga B, Albuquerque C D, Croft S L, Dumas M & Périé J, *J Med Chem*, 46 (2003) 427.
60 Carvalho S, Salomão K, Castro S L, Conde T R, Zamith H P, Caffarena E R, Hall B S, Ilkinson S R & Boechat N, *Mem Inst Oswaldo Cruz*, 109 (2014) 315.
61 Enanga, Keita M, Chauvière G, Dumas M & Bouteille B, *Trop Med Int Health*, 3(9) (1998) 736.
62 Darsaud, Chvrier C, Bourdon L, Dumas M, Buguet A & Bouteille B, *Trop Med Int Health*, 9(1) (2004) 83.
63 Pires, "Pharmacokinetic Properties of Megazol," PKCSM Available at: https://biosig.lab.uq.edu.au/pkcsm/prediction_single/adme_1701355361.03 (Accessed: 30 November 2023).
64 Sourkes T l, Sloane F S B & Drujan B D, *AMA Arch Neurol,* 78 (1957) 204.